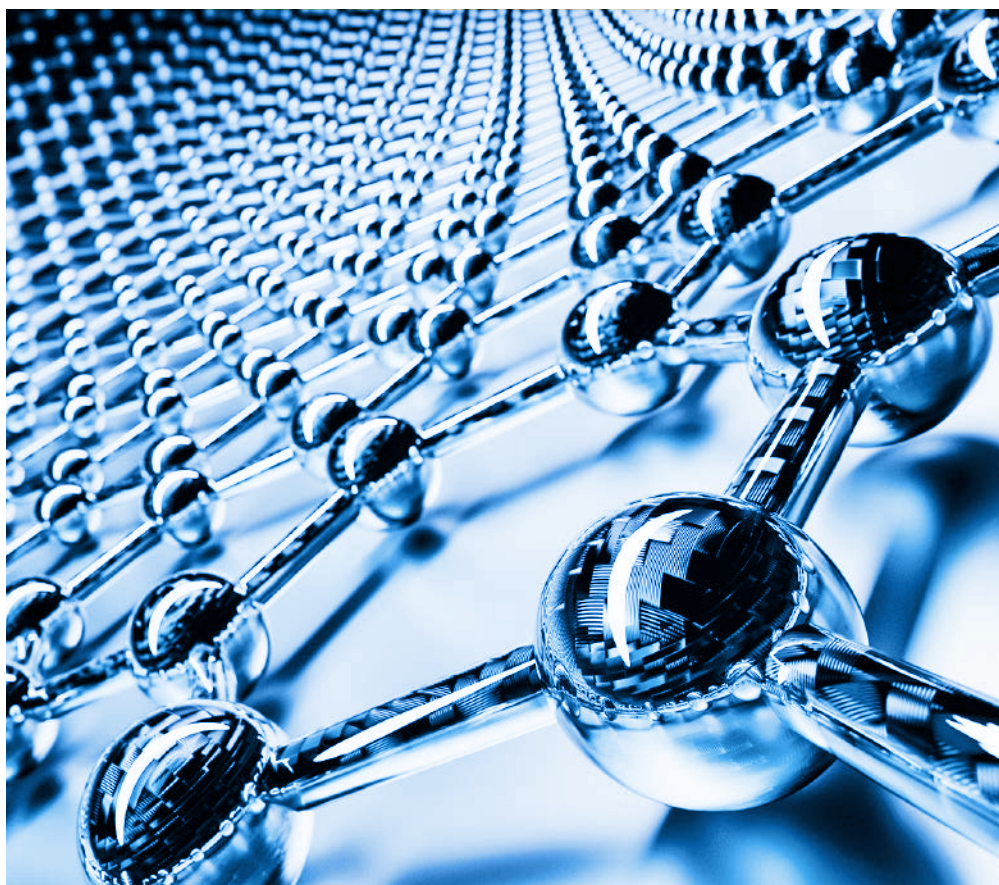
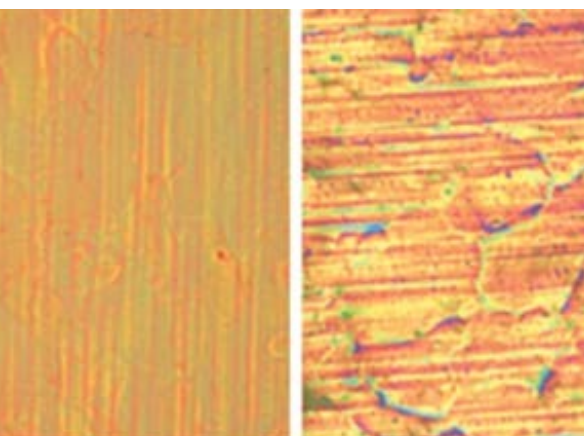
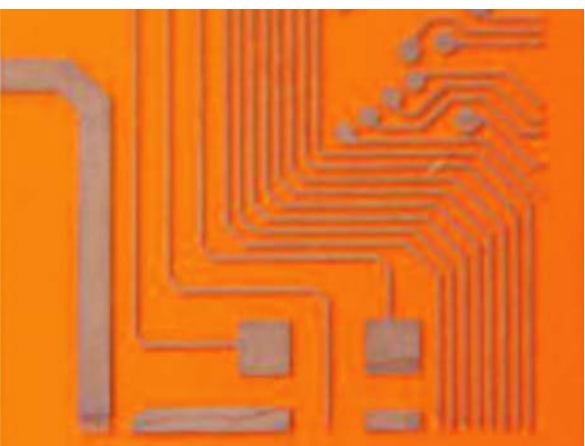


15

Optimizing Inter- face Conductivity in Electronics

—
LSM Characterization
of Surface Properties



Contents

- 3 Introduction
Optimizing interface conductivity in electronics:
LSM characterization of surface properties

- 5 A method for preparing crack- and wrinkle-free
wafer scale graphene
Adapted from Kim *et al.*

- 11 The influence of substrate surface roughness
on the losses of microstrip transmission lines
Adapted from Vincent *et al.*

- 18 Copper (Cu) nanoparticles for the fabrication of
conductive structures by ink-jet printing
Adapted from Jeong *et al.*

Imprint

© Wiley-VCH GmbH
Boschstr. 12,
69469 Weinheim, Germany
Email: info@wiley-vch.de
Editors:
Dr. Cecilia Kruszynski &
Róisín Murtagh

Optimizing interface conductivity in electronics: Laser scanning microscopy characterization of surface properties

The field of electronics has long been driven by semiconductors, materials that can conduct an electric current under certain conditions. Coupled with metals and insulators, semiconductors are the foundation of modern electronics, powering computers, lasers, smartphones, and many other devices. Of particular importance is the transistor, a device that revolutionized electronics and relies on the interfaces between semiconductors, metal, and insulators. Ensuring efficient charge transport across the metal-semiconductor interface is a major challenge for electronic device designers.

Besides transistors, many other electronic devices rely on different kinds of interfaces for their operation, for example, solar cells or devices that generate photons, microwaves, or acoustic waves. These devices require low-resistance contacts to inject current or apply voltage to the layer that generates the radiation. Otherwise, power is lost at these contacts, reducing or blocking power conversion within the electronic materials. Moreover, flat material/air interfaces are often required to ensure homogeneity in the current transport between them.^[1]

In recent years, increasing attention has been devoted to the development of convenient and low-cost processing techniques to fabricate conductive features such as electrodes, conductive lines, and interconnects for use in various electronic applications, as well as post-processing methods to improve surface properties.^[2-4] The new trend in fabrication and microfabrication aims to achieve cost-effective manufacturing, fast production cycles, shorter time-to-market, and environmentally

friendly practices. One of the most explored methods in this regard is inkjet printing of ink formulations based on metal nanoparticles, carbon nanotubes, and graphene sheets.^[2] This method has proven useful to fabricate conductive flexible devices.^[3,4]

Assessing the performance of a given material for its electronic application is key to evaluating its surface quality, and one central parameter in this regard is surface roughness. It is important to quantitatively assess roughness to compare production and finishing methods and to improve these methods based on mathematical models. One powerful tool to measure surface roughness is 3D laser scanning confocal microscopy (LSM).

LSM allows for a visual evaluation of surface conditions. It consists of scanning the sample surface with a microscope that employs a laser beam to acquire 3D data. For example, some Olympus microscopes are paired with a dedicated LEXT objective lens that adapts to the wavelength of the laser and

suppresses aberrations. This enables the system to capture fine patterns and defects that are difficult to capture with conventional optical microscopes and general laser microscopes. The optical system is also non-contact, so soft samples, like films, can be handled without concern for surface damage.

When evaluating roughness through microscopy it is important to use the right objective lens to be sure about the accuracy of the results. However, this is not an easy task. Fortunately, tools like the Smart Lens Advisor from Olympus can help. This software makes it easier to choose the right lens. Simply provide some basic information such as the field of view and the intended lens to use and the Smart Lens Advisor will display how suitable a given lens is for the application. This reduces the chance of using the wrong objective lens and having to run the experiment again with a different lens.

Whatever LSM you use, it is important that it can acquire the required roughness measurements. When evaluating roughness parameters, the practical quantification measures are the root mean square height (S_q), maximum height (S_z), and arithmetic mean height (S_a), which indicates the disproportion size relative to the average surface. Other equally important parameters are the expanded interface area ratio (S_{dr}), which accounts for the rate of increase in the surface area. Finally, the autocorrelation length (S_{al}) focuses on the lateral direction, such as the density of streaks and particles. A smaller S_{al} indi-

cates a steeper shape and finer grain. In contrast, a larger S_{al} indicates that the surface has a more gradual uneven shape.

In conclusion, when aiming to create high-conductivity electronic devices with minimal power loss and optimal performance, special focus must be placed on their interfaces. Generally, a smoother surface is preferable to reduce power loss; however, in certain scenarios, a rougher surface may be required for better anti-static properties. In any case, characterization of the surfaces is necessary to understand the optimal surface for a given application, for which laser scanning microscopy is an effective tool to discern a variety of roughness parameters and make an informed decision.

REFERENCES

- [1] Brillson, L.J. (2016). *Why Surfaces and Interfaces of Electronic Materials*, in *An Essential Guide to Electronic Material Surfaces and Interfaces*, John Wiley & Sons, Ltd, Chichester, UK, pp. 1–13. DOI: 10.1002/9781119027140.ch1
- [2] Kamyshny, A. and Magdassi, S. (2014). *Conductive Nanomaterials for Printed Electronics*. *Small*. DOI: 10.1002/smll.201303000
- [3] Sun, J. et al. (2022). *Fabricating flexible conductive structures by printing techniques and printable conductive materials*. *Journal of Materials Chemistry C*. DOI: 10.1039/D2TC01168A
- [4] Saidina, D.S. et al. (2019). *Recent Development of Graphene-Based Ink and Other Conductive Material-Based Inks for Flexible Electronics*. *Journal of Electronic Materials*. DOI: 10.1007/s11664-019-07183-w

01 A method for preparing crack- and wrinkle-free wafer-scale graphene

➔ Adapted from Kim, H.H. *et al* (2016)

INTRODUCTION

Graphene grown by chemical vapor deposition (CVD) has been extensively studied for its utility in industrial applications across a range of fields.^[1,2] The drawback of using CVD graphene grown on a metal catalyst is that during transfer onto a target substrate, a significant number of defects may be generated in the graphene, such as micrometer-scale cracks and wrinkles, which deteriorate both the uniformity and the quality of the graphene. The transfer of CVD-grown large-area graphene onto a target substrate without the formation of cracks and/or wrinkles remains a significant challenge in graphene research.^[3]

Recent problematic issues in graphene transfer include (i) the development of a transfer process onto an arbitrary substrate for diverse applications,^[2-4] and (ii) the reduction of uncontrolled deformations in graphene.^[5,6] Conventional methods for transferring CVD-grown graphene may be categorized as wet^[5,9,10] or dry^[9,10] methods. Both types of transfer suffer from critical weaknesses that result in transfer-induced defects, such as folds and cracks.

Herein, we report a simple and broadly applicable transfer method that uses organic liquids with low surface tensions for laminating defect-free graphene onto arbitrary substrates, even onto a strongly hydrophobic substrate.

RESULTS AND DISCUSSION

Figure 1a depicts the procedure used to transfer wrinkle- and crack-free graphene using our method. Graphene was grown on a copper (Cu) foil via CVD under the growth conditions described previously.^[1-3] A poly(methylmethacrylate) (PMMA) solution was spin-coated onto the graphene as a supporting layer (100 nm), and the Cu foil was etched away using an ammonium persulfate solution, followed by rinsing in deionized (DI) water. As shown in **Figure 1b**, conventional wet transfer methods^[2,3] were used to transfer the PMMA/graphene film directly onto the target substrate from DI water, but the PMMA/graphene film was transferred onto a suspending holder before the transfer onto a target substrate in this method. A small volume (2 μL) of a volatile liquid, such as heptane, was dropped onto the target substrate, followed by contacting the suspending

holder and cutting the edge. As evaporation proceeded, the PMMA/graphene film was transferred to the substrate spontaneously. After removing the holder and PMMA, the defect-free and uniform graphene was successfully transferred. The organic liquid (OL) transfer method was used with a large suspending holder to transfer a large-area wrinkle- and crack-free graphene film onto a 6 in. SiO_2/Si wafer. Compared with conventional transfer methods, the organic liquid transfer method did not generate lamination wrinkles and/or cracks even on the hydrophobic surface after the removal of PMMA (**Figure 1c**). By contrast, conventional wet transfer methods produced folds and cracks in the graphene within the local region in which lamination-induced wrinkles were formed as the supporting layer was removed after the transfer, as confirmed in the confocal laser scanning microscopy (CLSM) and optical microscopy (OM) images (**Figure 1d**).

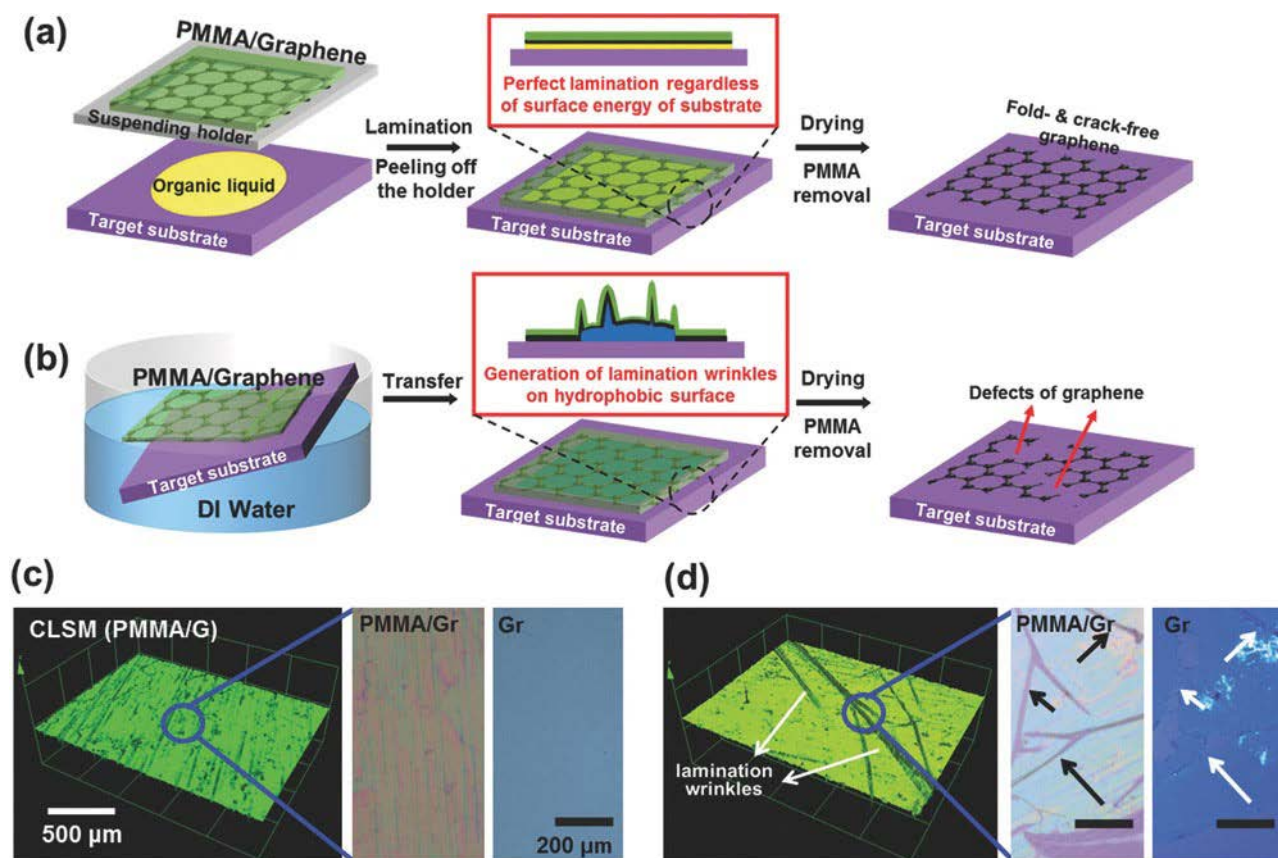


Figure 1: Schematic diagram showing, a) the organic liquid transfer and, b) the conventional wet transfer method. CLSM and OM images of a PMMA/graphene film and the final graphene layer obtained by c) organic liquid transfer, or by d) conventional wet transfer methods.

The mechanism underlying the generation of lamination wrinkles with different surface tensions of contacted liquid was investigated by analyzing the transfer processes of the PMMA/graphene films onto low surface energy substrates. In the case of organic liquids (e.g., heptane) with low surface tensions, the liquid droplets first fully spread between the substrate and the PMMA/graphene film. The pinned three-phase (solid–liquid–gas) contact line (TCL) of the liquid was located at the edge (or outside) of the film, which smoothed out any preformed wrinkles (that possibly arose as the film was transferred to the holder) due to an evaporation-induced internal flow directed toward the TCL.^[4,5] In addition, as the thin liquid layer evaporated, the gap between the PMMA/graphene film and the substrate decreased overall, and finally, the film contacted the substrate at the same time. As a result, the transferred PMMA/graphene film

was extremely flat without lamination wrinkles. Meanwhile, the generation of local wrinkles might be affected by the evaporation rate of the liquid. However, the ratio of the actual area to the projected area of the film would not be changed. If the evaporation rate of the liquid is extremely high, it can affect the contact between the film and the substrate, which results in the formation of wrinkles. In the case of the organic liquid transfer method, the evaporation takes place through the small gap between the film and the substrate, which results in a slower evaporation rate than expected despite the high vapor pressure.

The PMMA/graphene film transferred using water with a high surface tension, by contrast, displayed lamination wrinkles due to the trapped water with a high contact angle between the film and the substrate. As the PMMA/graphene film was transferred onto the

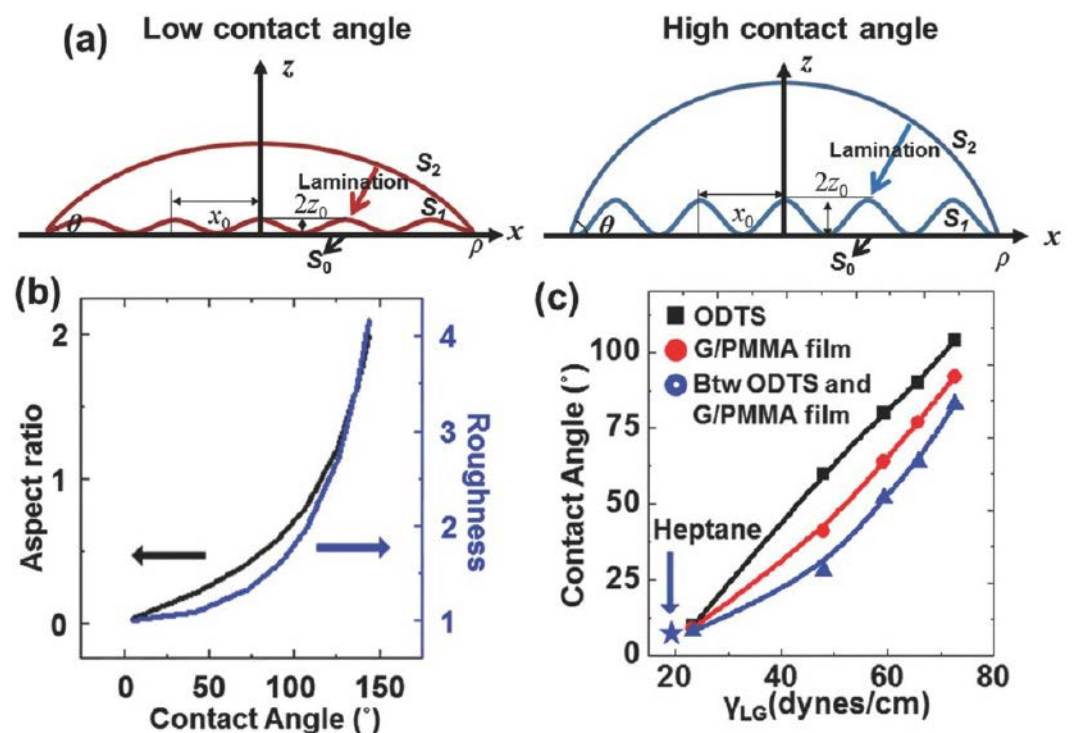


Figure 2: a) Model of the lamination wrinkles (S_1) induced by low (red) or high (blue) contact angle (θ) liquids trapped between the PMMA/graphene film (S_2) and the substrate (S_0). After drying liquids, S_2 becomes S_1 . b) Computed values of the aspect ratio ($2z_0/x_0$) of the lamination wrinkles and the roughness ratio (R) as a function of the contact angle (θ) of the trapped liquids. c) Contact angles of liquid with different surface tensions on the ODTS-treated SiO_2/Si substrate, graphene/PMMA film, and between the ODTS-treated SiO_2/Si substrate and the film.

substrate, the water droplet initially bent the film toward the substrate, which was wrapped by a thin flexible film. This spontaneous wrapping of the film, which converted the liquid–air and solid–air interfaces into solid–liquid and solid–solid interfaces, was attributed to a reduction in the surface energy at the cost of increasing the isometric bending energy in the flexible film.^[6] As the trapped water evaporated through the pinned TCL (solid–liquid–gas), the film was pulled around the water droplet center, which produced biaxial compressive strain in the film layer. High compressive strains caused localized contact and crumpling of the film on the substrate, resulting in non-uniform lamination wrinkles.^[7,8] The lamination wrinkles of the film were converted into folds or cracks of graphene, which greatly reduced the performances of the resulting graphene devices after the removal of the PMMA supporting layer. Minimizing lamination wrinkles in a PMMA/graphene film is the best way to decrease defects and obtain uniform high-quality graphene.

Theoretical calculations and systematic studies were performed to examine the correlation between the topography of the lamination wrinkles and the contact angle of the transfer medium. It was demonstrated that the contact angle θ , and a roughness ratio R (**Figure 2**) may be numerically calculated for the aspect ratio of the wrinkles. The aspect ratio of the wrinkles and R decreased as θ decreased. Interestingly, for extremely small values of θ , the surface of the film did not wrinkle (i.e., $R \sim 0$). These conditions corresponded to the absence of lamination wrinkles observed previously using the organic liquid transfer method.

The theoretical results were corroborated by measuring θ and examining the topography of the lamination wrinkles in the transferred PMMA/graphene films as a function of the transfer liquid surface tension, which was tuned by mixing IPA and DI water. The theoretical model calculations and experimental results indicated that the low contact angle of the liquid with a low surface tension could prevent PMMA/graphene films from forming lamination wrinkles during the transfer process.

Heptane was selected as a low surface tension liquid ($19.3 \text{ dynes cm}^{-1}$) that enabled the PMMA/graphene film to be homogeneously laminated owing to its complete wetting on all investigated substrates. Although the target

substrate was hydrophobic, heptane spread readily on this substrate because its surface tension was lower than the critical surface tension needed to initiate spreading. We verified the critical surface tension of the transfer medium needed on the ODTs-treated SiO_2/Si substrate using Zisman's method.^[9] The critical surface tension of the liquid was obtained by plotting the cosine of the contact angle on the substrate with the surface tension of the transfer medium.

Graphene transferred onto polymeric substrates is widely investigated for use in flexible optoelectronics devices because they offer excellent flexural resistance.^[2,10,11] The hydrophobicity of the polymeric substrates, however, inevitably produces transfer defects in the graphene.^[12] The organic liquid transfer process allows for the transfer of defect-free graphene films onto many polymeric substrates, such as polyethylene terephthalate (PET) and poly(dimethylsiloxane). This method was used to fabricate laminated wrinkle-free PMMA/graphene films on hydrophobic PET substrates that had been treated with CF_4 plasma and on which the heptane contact angle was extremely small. Conventional wet transfer processes, however, produced lamination wrinkles in the PMMA/graphene film on the CF_4 -treated PET substrate due to the large contact angle of water. The mechanical flexibility of the graphene/PET film after the removal of the PMMA supporting layer was evaluated by submitting the films to repeated bending cycles at a radius of 5 mm. After 500 bending–unbending cycles, the conductance of the organic liquid-transferred graphene remained relatively stable (decreased by 10%), in contrast to the conventional wet-transferred graphene, which did not survive the process (the conductance decreased by 90%). This remarkable difference resulted from the propagation of graphene cracks during bending.

Because the graphene that had been initially transferred using an organic liquid with a low surface tension had no folds and/or cracks, only a low number of defects were generated after bending. Graphene transferred using the wet transfer method, however, displayed a high density of cracks formed along the lamination wrinkles and cracks during bending. As a result, the initial defects in the transferred graphene primed the graphene film for destruction, and its electrical and mechanical properties degraded.

CONCLUSION

In conclusion, the lamination wrinkles formed in PMMA/graphene films and induced by the high contact angle of the trapped transfer medium liquid between the film and the substrate are investigated by experimental and theoretical approaches. Moreover, it is demonstrated that the lamination wrinkles can be converted into folds and cracks in the graphene after removing the PMMA supporting layer, which reduces the performance of the graphene film in applications. The results support the utility of a novel transfer method using volatile liquids with low surface tensions (e.g., heptane) that can spread readily over a variety of solid surfaces, regardless of the surface energies. This method minimizes lamination wrinkles to yield high-quality graphene on a variety of substrates. The graphene transferred using the proposed method is uniform, can be used to fabricate high-mobility GFETs, and displays excellent mechanical resilience against bending. These transfer techniques and analyses provide a solution to the fundamental problems facing CVD-grown graphene commercialization and may offer new opportunities for enhancing the quality and uniformity of 2D materials in a variety of functional devices.

EXPERIMENTAL SECTION

Transferring graphene using the transfer medium liquid: After the growth of monolayer graphene on a copper foil using chemical vapor deposition, followed by spin-coating of a polymethylmethacrylate film, the back side of the graphene was removed by reactive ion etching using oxygen plasma. The PMMA/graphene/copper foil film was floated on the surface of an aqueous solution containing 0.1 M ammonium persulfate ($(\text{NH}_4)_2\text{S}_2\text{O}_8$) to remove the copper foil, and the PMMA/graphene films were transferred to deionized water. The floated films were transferred to a suspended holder (120 μm thick PET) and were dried in a vacuum oven at 60 $^\circ\text{C}$ (140 $^\circ\text{F}$). The dried films were transferred onto the target substrate after depositing a droplet of the transfer medium liquid with a low surface tension, such as heptane, and the edges were cut off to remove the suspended holder from the substrate. The samples were baked at 120 $^\circ\text{C}$ (248 $^\circ\text{F}$), and the PMMA was removed by acetone.

Characterization: The transferred graphene films were characterized by optical microscopy, confocal laser scanning microscopy (LEXT

OLS3100, Olympus), atomic force microscopy, field-emission scanning electron microscopy, Raman spectroscopy, and semiconductor parameter analyzer.

REFERENCES

- [1] Xue, Y. et al. (2014). *Controllable Synthesis of Doped Graphene and Its Applications*. *Small*. DOI: 10.1002/SMLL.201400706.
- [2] Kim, G. et al. (2015). *Catalytic Conversion of Hexagonal Boron Nitride to Graphene for In-Plane Heterostructures*. *Nano Letters*. DOI: 10.1021/ACS.NANO.5B01704/SUPPL_FILE/NL5B01704_SI_001.PDF.
- [3] Kang, J. et al. (2012). *Graphene transfer: key for applications*. *Nanoscale*. DOI: 10.1039/C2NR31317K.
- [4] Caldwell, J.D. et al. (2010). *Technique for the dry transfer of epitaxial graphene onto arbitrary substrates*. *ACS Nano*. DOI: 10.1021/NN901585P/SUPPL_FILE/NN901585P_SI_001.TIF.
- [5] Reina, A. et al. (2009). *Large area, few-layer graphene films on arbitrary substrates by chemical vapor deposition*. *Nano Letters*. DOI: 10.1021/NL801827V/SUPPL_FILE/NL801827V_SI_003.PDF.
- [6] Gao, L. et al. (2013). *Face-to-face transfer of wafer-scale graphene films*. *Nature* 2013 505:7482. DOI: 10.1038/nature12763.
- [7] Wei, D. et al. (2009). *Synthesis of n-doped graphene by chemical vapor deposition and its electrical properties*. *Nano Letters*. DOI: 10.1021/NL803279T/SUPPL_FILE/NL803279T_SI_001.PDF.
- [8] Liang, X. et al. (2011). *Toward clean and crackless transfer of graphene*. *ACS Nano*. DOI: 10.1021/NN203377T/SUPPL_FILE/NN203377T_SI_002.AVI.
- [9] Li, X. et al. (2009). *Large-area synthesis of high-quality and uniform graphene films on copper foils*. *Science*. DOI: 10.1126/SCIENCE.1171245/SUPPL_FILE/LI.SOM.PDF.
- [10] Gao, L. et al. (2012). *Repeated growth and bubbling transfer of graphene with millimetre-size single-crystal grains using platinum*. *Nature Communications* 2012 3:1. DOI: 10.1038/ncomms1702.
- [11] Bae, S. et al. (2010). *Roll-to-roll production of 30-inch graphene films for transparent electrodes*. *Nature Nanotechnology* 2010 5:8. DOI: 10.1038/nnano.2010.132.
- [12] Kang, J. et al. (2012). *Efficient transfer of large-area graphene films onto rigid substrates by hot pressing*. *ACS Nano*. DOI: 10.1021/NN301207D/SUPPL_FILE/NN301207D_SI_001.PDF.
- [13] Lee, W.H. et al. (2011). *Control of Graphene Field-Effect Transistors by Interfacial Hydrophobic Self-Assembled Monolayers*. *Advanced Materials*. DOI: 10.1002/ADMA.201101340.

- [14] Lee, W.H. et al. (2011). *Transparent Flexible Organic Transistors Based on Monolayer Graphene Electrodes on Plastic*. *Advanced Materials*. DOI: 10.1002/ADMA.201004099.
- [15] Lee, W.H. et al. (2011). *Surface-directed molecular assembly of pentacene on monolayer graphene for high-performance organic transistors*. *Journal of the American Chemical Society*. DOI: 10.1021/JA1097463/SUPPL_FILE/JA1097463_SI_001.PDF.
- [16] Deegan, R.D. et al. (1997). *Capillary flow as the cause of ring stains from dried liquid drops*. *Nature* 1997 389:6653. DOI: 10.1038/39827.
- [17] E B Dussan, V. (2003). *On the Spreading of Liquids on Solid Surfaces: Static and Dynamic Contact Lines*. <http://dx.doi.org/10.1146/annurev.fl.11.010179.002103>. DOI: 10.1146/ANNUREV.FL.11.010179.002103.
- [18] Py, C. et al. (2007). *Capillary origami: Spontaneous wrapping of a droplet with an elastic sheet*. *Physical Review Letters*. DOI: 10.1103/PHYSREVLETT.98.156103/FIGURES/5/MEDIUM.
- [19] (1957). *Folding instability of a layered viscoelastic medium under compression*. *Proceedings of the Royal Society of London. Series A. Mathematical and Physical Sciences*. DOI: 10.1098/RSPA.1957.0187.
- [20] Pocivavsek, L. et al. (2008). *Stress and fold localization in thin elastic membranes*. *Science*. DOI: 10.1126/SCIENCE.1154069/SUPPL_FILE/POCIVAVSEK.SOM.PDF.
- [21] Kabza, K. et al. (2000). *Contact Angle Goniometry as a Tool for Surface Tension Measurements of Solids, Using Zisman Plot Method. A Physical Chemistry Experiment*. *Journal of Chemical Education*. DOI: 10.1021/ED077P63.
- [22] Kim, H.H. et al. (2014). *Water-Free Transfer Method for CVD-Grown Graphene and Its Application to Flexible Air-Stable Graphene Transistors*. *Advanced Materials*. DOI: 10.1002/ADMA.201305940.
- [23] Eda, G. et al. (2008). *Large-area ultrathin films of reduced graphene oxide as a transparent and flexible electronic material*. *Nature Nanotechnology* 2008 3:5. DOI: 10.1038/nnano.2008.83.

02 The influence of substrate surface roughness on the losses of microstrip transmission lines

➔ Adapted from Vincent, T. *et al* (2009)

INTRODUCTION

Avoiding transmission losses is crucial in telecommunications since high conductor losses can lead to signal attenuation and to subsequent expensive amplification. However, mitigating electromagnetic losses can be challenging unless the mechanisms and impact of loss components are fully understood.

The electrical loss of a copper wire at GHz frequencies depends on the surface treatments to which the copper had been subjected.^[1] Hammerstad developed an empirical equation to estimate transmission loss, which is still widely used.^[2] However, this equation has limitations, as it does not accurately determine transmission loss over a wide surface topography or frequency range.^[3] Moreover, transmission loss does not follow a square root of frequency relationship.^[4,5]

This study examines the measurements of microwave-frequency transmission loss of microstrip conductive lines with three different lengths on substrates with four different surface finishes. The research shows that three of the substrate surfaces have statistically significant differences over certain scale ranges, as determined by average roughness (R_a) and length-scale fractal analysis.^[6]

THEORY

A microstrip conductor line – a thin, flat electrical conductor separated from the electrical ground plane by an insulating layer – has two topographies that significantly affect conductor loss, the conductor-ceramic interface and conductor edge angle. Both topographies can be influenced by the roughness of the substrate surface. As frequency increases, the skin effect forces the signal to follow the surface profile more closely, causing the signal to concentrate at the conductor edges.^[7]

The skin effect is a phenomenon where the current in the propagating signal decays exponentially with distance from the ceramic-conductor interface into the conductor. This effect is a function of the operating frequency (f), conductivity (σ) of the path trace and material permeability (μ), as expressed by Equation (1), where the single skin depth (δ_s) is defined as the depth at which the current density has decreased to $1/e$ ($\approx 37\%$) of its surface value. This effect is central to our understanding of why surface roughness affects conductor loss.

At GHz frequencies, circuits of this type have several loss components, including reflected loss, dielectric loss, and conductor loss. The total loss is represented as the incident signal minus the resultant signal, divided by the incident signal, expressed in decibels. The transmission loss is the total loss minus the reflected loss, and it is made up of the conductor loss and dielectric loss components.

Here, the electrical samples were fabricated using thick-film technology, which is a common method for microelectronics. This allowed the circuits to be fabricated on a substrate with negligible dielectric losses. Therefore, the major transmission loss is due to conductor loss.

$$\delta_s = \sqrt{\frac{1}{\pi f \sigma \mu}} \quad (1)$$

The average roughness R_a and peak-to-peak height of the profile (R_t) have frequently been used as parameters to characterize the roughness of surfaces for electrical applications.^[8] R_a is defined as

$$R_a = \frac{1}{L} \int_0^L |Z(x)| dx \quad (2)$$

where $Z(x)$ is the deviation of the roughness profile from the mean line of the profile, and L is the evaluation length of the profile.^[6]

While R_a and R_t are widely used to describe surface roughness, they have limitations when it comes to characterizing the electrical behavior of surfaces. These parameters do not take into account the distribution of surface heights or their impact on the electrical path length at a particular frequency or scale. They are also insensitive to the spatial distribution of the surface heights. In addition, R_a and R_t are unable to differentiate between a single significant peak and multiple smaller peaks, which contribute likewise. Similarly, a valley or peak of the same magnitude will have the same effect on R_a values, regardless of their location within the measurement field.

The surface roughness of a conductor increases the length of the current path, leading to an increase in conductor loss per unit length. This loss increases at a rate proportional to the square root of frequency. However, as the skin depth and surface roughness scales become comparable, the loss increases at a higher rate than the square root of frequency. The additional loss caused by surface roughness can be estimated using the conventional equation (2) that represents the resultant conductor loss, α_c :

$$\alpha_c = \alpha_{smooth} \left\{ 1 + \frac{2}{\pi} \arctan \left[1.4 \left(\frac{R_a}{\delta_s} \right)^2 \right] \right\} \quad (3)$$

Equation (3), developed by Hammerstad, calculates the surface roughness contribution to conductor-ceramic interface loss for traces at least five skin depths thick. Conductivity solely determines the loss for lines thinner than one skin depth, whereas the primary loss component for lines at least five skin depths thick is due to the skin effect. For lines between one and five skin depths thick, the loss component is transitional and involves both the skin effect and surface roughness contribution.

In this study, the specimen used was made of a silver alloy, and five skin depths would correspond to a frequency of 7 GHz. Interestingly, at this frequency, the measured transmission loss starts to diverge from the Hammerstad calculation, as depicted in **Figure 1**. Therefore, while Equation (3) was originally meant to be able to account for the surface roughness effect on conductor loss, it does the opposite at the very frequency where it should be applicable.

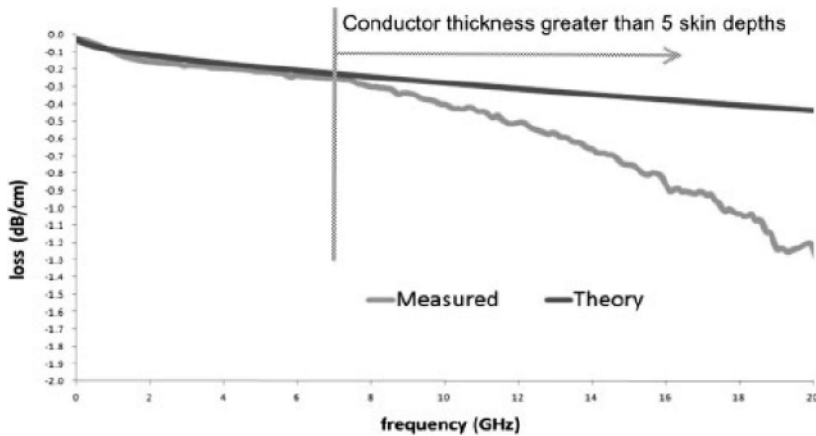


Figure 1: Comparing measured conductor loss from a lapped surface with the theoretical loss derived from Equation (3).

Table 1: Surface finish processes description with average roughness result

Surface finish process	Process descriptions	R_a (μm)
Lapped	Lapped using an oil-based abrasive; cleaned in ultrasonic bath and rinsed with alcohol (ACUMET)	0.18
Vapor honed	Blasted with 220 grit aluminum oxide and water, then vapor honed for 2.5 min with 12.5 μm (0.5 mil) of material removed	0.56
Sintered	After vapor hone, placed in a furnace for a sintering cycle	0.55
Chemically etched	Held in an Anodex solution for 1 h at 150 °C (302 °F), then in an HCl solution for 1 h at 150 °C, followed by cold water rinse. This process is repeated twice	1.09

Fringing fields increase current density at the conductor edge, which can be further intensified by sharper corners.^[9] During thick-film printing, the substrate surface's rough peaks or slopes hinder the lateral movement of the conductor paste, causing larger cross-sectional edge angles and tapered edges. Consequently, thick-film conductors have a higher current density at their edges than square cross-section conductors.

For circuits made by thick-film processing, the conductor edges are not perpendicular but angled.^[10] The angle of the conductor edge depends on the substrate surface pro-

cess. For rougher surfaces, due to the paste rheology, the conductor edge has a wider angle.^[11] As the substrate surface becomes smoother, the edge becomes smoother as well.

Characterization of surface roughness by length-scale analysis

Scale-sensitive fractal analysis has proven useful in statistically discriminating rough surfaces and finding correlations with surface behavior in various applications, including optical scattering.^[6,12–14] It enables length-scale fractal analysis to statistically discriminate surfaces where R_a measurement is insufficient.^[15]

Length-scale fractal analysis calculates profile lengths by virtually stepping along the surface with progressively shorter step sizes. Longer profile lengths are obtained at smaller scales, as they follow the surface profile more closely. This explains conductor loss as the relative slope increases with decreasing scale.

The length-scale fractal analysis uses a step size referred to as the scale of observation or calculation. The relative length is obtained by dividing the measured length at a scale by the nominal length, which is a straight line.

EXPERIMENTAL PROCEDURES

Substrate production and profile measurement

Four different substrate surface roughness were created on aluminum nitride (AlN) substrates using four different surface finish processes as described in **Table 1**. All the surfaces had previously been vapor honed.

The surface finishes were evaluated by taking six height profiles (z as a function of x) using a Perthen (Mahr Federal) profiler with an unskidded stylus having a tip radius of 2 μm . The profiles were taken with a sampling interval of 69 nm and a trace length of 560 μm . The profiles were then processed using Gaussian filtering with a wavelength cut off 0.08 mm. The surface finish was characterized using arithmetic average roughness (R_a) and length-scale fractal analysis as per ASME B46 2002 standards. The Map Premium software (Digital Surf) and Sfrax were used for analyzing the measured profiles.

The results of the roughness characterization (**Table 1**) show that the surface finish

process has a significant effect on the surface roughness of the AlN substrates.

The conductor edge measurements

The conductor edge was measured for the silver conductor (ALN11) and silver/palladium conductor (ALN33) samples using an interferometric microscope. Note that upper case L in 'ALN' is used to denote the conductor pastes on the AlN substrates.

The conductor line measurements

Thick-film screen-printing technology was used to make the microstrip circuits for this study. Six substrate plates were printed with microstrip circuits. Two specimens of each substrate finish were printed with each type of conductive paste (see below).

- ALN 11 © [DuPont 2001] a silver conductor
- ALN 33 © [DuPont] a silver/palladium conductor (10:1)
- ALN 23 © [DuPont] silver/platinum conductor (3:1)

The study used two sets of microstrip circuits on each plate, with each set containing three conductor lines of different lengths; the longest line was used for loss measurements. A serpentine line on each plate was used to measure bulk conductivity. Loss measurements were taken using an Anritsu Vector Network Analyzer and picoprobes, calibrated with substrate standards. Reflected losses were measured and subtracted from total loss to calculate the transmission loss. SONNET software was used to analyze the loss measurements,

and regression analysis was conducted at selected frequencies to compare loss measurement and profile characterizations.

Transmission line equations were used to calculate reflected loss caused by mismatches between the input/output transition and conductor line. Reflected losses are design-dependent and subtracted from the total loss to determine transmission loss. Three conductor line lengths were used to measure and validate transmission losses. Regression analysis compared loss measurements and profile characterizations at each length-scale and frequency, plotted as regression coefficient versus scale determined by length-scale analysis.

Table 2 displays the conductivities of the three ALN microstrip conductor lines and pure silver. The skin depth for bulk conductivity and frequency is calculated using Equation (1).

RESULTS

Surface roughness characterization

Measurements were taken of substrate surfaces treated with chemical etching, vapor honing, and lapping using a LEXT OLS3100 scanning laser confocal microscope from Olympus (**Figure 2**). The length-scale fractal analysis showed that the relative lengths of the profiles were similar at scales above 100 μm and increased rapidly with a decrease in scale between scales of about 2 μm and 20 μm . The chemically etched surface had a longer path length than all other surfaces at scales below 50 μm , while the lapped surface had a shorter path length at scales below 30 μm . The length-scale roughness

Table 2: Skin depth for conductor lines with different conductivities

Conductor line	Measured d.c bulk conductivity (S/m)	Skin depth (μm)				
		100 MHz	1 GHz	10 GHz	15 GHz	20 GHz
Silver ^a	6.2×10^7	6.35	2	0.64	0.52	0.45
ALN11	2.2×10^7	10.75	3.4	1.08	0.89	0.76
ALN33	6×10^6	19.56	6.18	1.96	1.6	1.38
ALN23	8×10^5	56.27	17.79	5.63	4.59	3.98

^a Pure silver was not tested here and appears in this table to provide a reference for comparison.

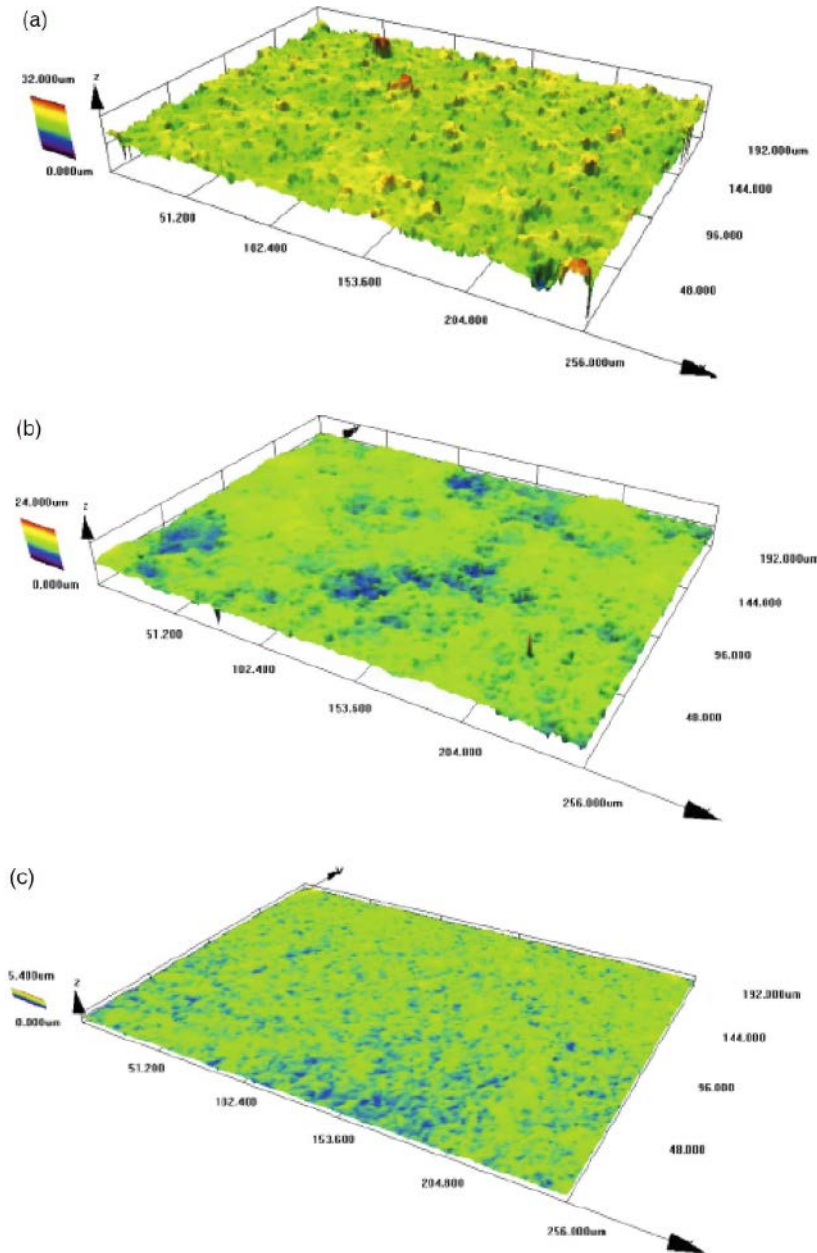


Figure 2: (a) Height map measurement of chemically etched surface. (b) Height map measurement of honed surface. (c) Height map measurement of lapped surface.

characterizations of profiles from the four different substrate surface treatments were shown with F-tests performed on all six measurements, indicating that all surface comparisons were discernable for scales less than 60 μm except for the vapor honed and sintered surface comparison.

Transmission loss versus frequency for four surfaces

The AlN substrate surface finishes' conductor losses were studied with different conductivity lines. For the high and intermediate conductivity lines, the conductor loss results were similar for all four substrate finishes over the low frequency range but started to disperse around 9-11 GHz. Notably, the rank of the losses did not correspond to the average roughness or the relative lengths at any scale shown in the results. The chemically etched AlN substrate provided the smallest losses, while the lapped AlN substrate resulted in the greatest transmission loss. The lowest conductivity line had more similar loss results for all four substrate finishes. For this line, the chemically etched AlN substrate with the greatest roughness provided the greatest losses up to frequencies of approximately 18 GHz, while the lapped AlN substrate, which was the smoothest, had the greatest loss.

Correlation of loss with R_a

Conductor loss in decibels at four discrete frequencies was measured for all four surface finishes and for all three-conductor conductivities as a function of average roughness, R_a . The results showed that at lower frequencies (5 GHz and 10 GHz), the loss did not depend on the frequency. At the highest frequency (20 GHz), the correlation between the loss and roughness was negative, with the smoothest surface having the greatest loss and the roughest surface having the smallest loss. This negative correlation was also observed for conductor loss as a function of R_t , and for the intermediate frequencies for the ALN11 and ALN33 conductor lines. However, the ALN23 conductor line behaved somewhat differently due to its lower conductivity and larger skin depth. The two sets of loss measurements were very similar, differing by only a few hundredths of a dB at 20 GHz.

Correlation of loss with path length (i.e., relative length) at three scales and four discrete frequencies

Conductor loss trends are similar to roughness, as seen in plots of conductor loss versus relative length at specific frequencies. The study examined three conductors (ALN11, ALN33, and ALN23) at different scales of observation and surface finishes. At lower frequencies (5 and 10 GHz), the two better conductors exhibited similar loss values for all surface

finishes. However, at higher frequencies (15 and 20 GHz), the lapped surfaces had the largest losses, followed by sintered, honed, and chemically etched surfaces. ALN23 had a similar behavior, with the chemically etched surface having the greatest loss at 10 and 15 GHz.

Correlation of loss with conductor edge angle

The conductor edge angle was measured at different length scales for ALN11 and ALN3. There is a positive correlation between conductor edge angle and length scale, which becomes more pronounced as the scale decreases. A similar relationship exists between conductor edge angle and surface roughness. This suggests that the angle is influenced by the substrate surface roughness, causing a greater contact angle. As the frequency increases, a correlation between conductor edge angle and loss appears, distinct at 20 GHz.

DISCUSSION

It was found that the dominant factor affecting conductor loss is the conductor edge angle, which is influenced by surface roughness. Rougher surfaces with larger slopes and peaks result in larger conductor edge angles, which even out the current density at the edges and reduce loss. However, this paper challenges the common assumption that the conductor-ceramic interface roughness is the dominant factor affecting conductor topography.

The study also found that smoother surfaces exhibit greater loss at all conductivities and that the negative correlation between loss and relative lengths becomes stronger and more consistent at smaller scales. This suggests that loss is related to surface characteristics but not to the increased path length at higher frequencies.

The conductor edge profile, specifically the z-axis angle at the edges of the silver conductor line, could also affect loss, but analysis did not reveal any discernable difference between edge profiles for different surface roughness.

The study used peak-to-valley roughness, arithmetic average roughness, and relative lengths as surface characterization methods and found that they all provided similar rankings of surfaces with respect to treatments and similar abilities to discriminate. However, the correlation between loss

and these parameters depends on the particular set of surfaces being considered.

The relationship between conductor loss and surface roughness depends on conductor conductivity and operating frequency. Below 10 GHz, surface roughness has no effect on conductor loss, but at 20 GHz, all three conductor lines show dependency on it. Conductor loss increases with higher frequency and lower conductivity, but not in accordance with the Hammerstad equation. ALN23 conductor's loss rank differs from ALN11 and ALN33 only above 15 GHz due to the skin effect. Both conventional and length-scale methods can distinguish between surfaces, with finer scales providing better discrimination.

CONCLUSIONS

Microstrip configurations were produced on three AlN substrate surfaces with conductors of varying conductivity. Surface characterization using R_a , R_r , and length-scale fractal analysis showed the same ranking for all surfaces. Conductor loss was measured from dc to 20 GHz and showed an inverse correlation with R_a and length-scale relative length at 20 GHz. There was no evidence of increased path length causing greater conductor loss at higher frequencies, but surface roughness did have a negative correlation. Higher frequency and lower conductivity led to greater conductor loss, and rougher surfaces resulted in larger cross-sectional edge angles. Loss dependence on roughness varied with conductor and frequency.

REFERENCES

- [1] Morgan, S.P. (2004). *Effect of Surface Roughness on Eddy Current Losses at Microwave Frequencies*. *Journal of Applied Physics*. DOI: 10.1063/1.1698368.
- [2] Hammerstad, E. and Jensen, O. (1980). *ACCURATE MODELS FOR MICROSTRIP COMPUTER-AIDED DESIGN*. *IEEE MTT-S International Microwave Symposium Digest*. DOI: 10.1109/MWSYM.1980.1124303.
- [3] Vincent, T. et al. (2010). *The influence of substrate surface roughness on microstrip transmission line loss using conventional analyses and length-scale fractal analysis*. *Surface and Interface Analysis*. DOI: 10.1002/SIA.3133.
- [4] Brist, G. et al. *Non-Classical Conductor Losses due to Copper Foil Roughness and Treatment*.
- [5] Hall, S. et al. (2004). *Modeling requirements for transmission lines in multi-gigabit systems*. *IEEE Topical Meeting on Electrical Performance of*

- Electronic Packaging*. DOI: 10.1109/EPEP.2004.1407549.
- [6] (2002). ASME B46.1 Surface Texture (Surface Roughness, Waviness, and Lay). An American National Standard, Ch. 10.
- [7] Kennelly, A.E. et al. (1915). Experimental researches on skin effect in conductors. *Transactions of the American Institute of Electrical Engineers*. DOI: 10.1109/T-AIEE.1915.4765283.
- [8] Bayes, M. and Horn, A. (2004). Effects of conductor surface condition on signal integrity. *Circuit World*. DOI: 10.1108/03056120410520551/FULL/XML.
- [9] Meixner, J. (1972). The behavior of electromagnetic fields at edges. *IEEE Transactions on Antennas and Propagation*. DOI: 10.1109/TAP.1972.1140243.
- [10] T. Vincent, I.B.-O. (2008). Conductor edge definition influence on high frequency electrical loss. *Proc. MS&T 2008*.
- [11] Vincent, T.S. et al. (2010). Quantitative edge cross-section angle impact on conductor loss. *IEEE Transactions on Components and Packaging Technologies*. DOI: 10.1109/TCAPT.2010.2050380.
- [12] Brown, C.A. and Siegmund, S. (2001). Fundamental scales of adhesion and area-scale fractal analysis. *International Journal of Machine Tools and Manufacture*. DOI: 10.1016/S0890-6955(01)00057-8.
- [13] Narayan, P. et al. (2006). Differentiation of the surface topographies of pharmaceutical excipient compacts. *Materials Science and Engineering: A*. DOI: 10.1016/J.MSEA.2006.05.135.
- [14] SHIPULSKI, E.M. and BROWN, C.A. (2011). A SCALE-BASED MODEL OF REFLECTIVITY. <https://doi.org/10.1142/S0218348X94000557>. DOI: 10.1142/S0218348X94000557.
- [15] Jordan, S.E. and Brown, C.A. (2006). Comparing texture characterization parameters on their ability to differentiate ground polyethylene ski bases. *Wear*. DOI: 10.1016/J.WEAR.2005.12.011.

03 Copper (Cu) nanoparticles for the fabrication of conductive structures by ink-jet printing

➔ Adapted from Jeong, S., *et al* (2008)

INTRODUCTION

In recent years, increasing attention has been devoted to the development of convenient and low-cost processing techniques to fabricate conductive features such as electrodes, conductive lines, and interconnects for use in various electronic applications. Although photolithography has been widely adopted in the microfabrication of conductive features, it is time-consuming, complicated, and expensive. Therefore, there is a need for direct digital printing techniques that are simpler and less expensive. In this context, inkjet printing is a promising alternative to traditional lithography.^[1–3]

Metals that possess high conductivity and operational stability can be applied via inkjet printing in the form of nanoparticles in conductive inks. The metal nanoparticles contained in the printed pattern are then converted to conductive granular metal films via post-printing thermal annealing at much lower temperatures than the melting points of the corresponding bulk metals.

In this regard, copper is a good alternative material as it is highly conductive and significantly cheaper than gold (Au) and silver (Ag), for example. When Cu nanoparticles are synthesized on a large scale in an ambient atmosphere, the formation of a surface oxide layer on the Cu is inevitable because the oxide phases are thermodynamically more stable. The presence of copper oxides on the surfaces of nanoparticles has two negative consequences: it increases the annealing temperature required and reduces the electrical conductivity.

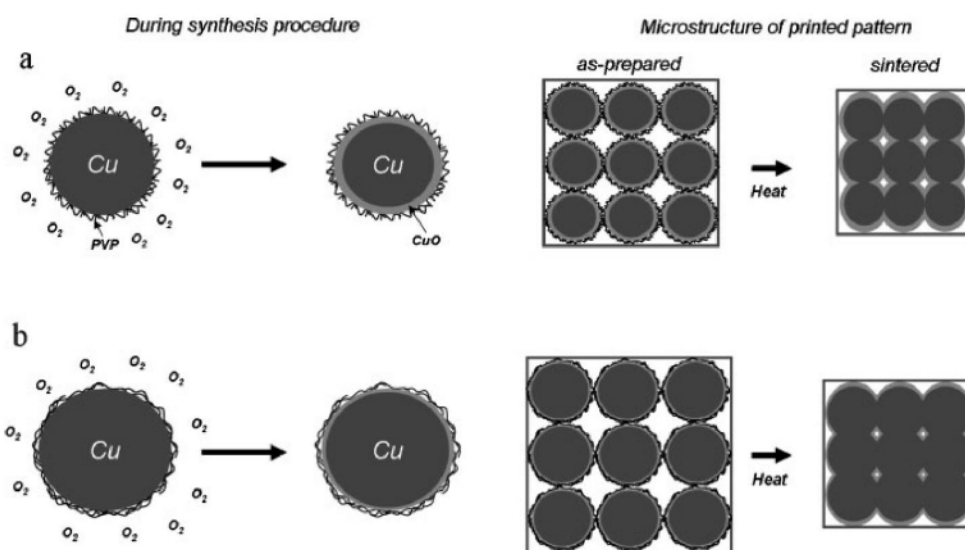


Figure 1: Schematic diagram representing the different conformations of the capping molecules chemisorbed on the surfaces of Cu nanoparticles synthesized using a) lower molecular weight PVP and b) higher molecular weight PVP. Also shown is the microstructural evolution of each particle type during sintering.

RESULTS AND DISCUSSION

Copper nanoparticles 35–60 nm in size were synthesized in an ambient atmosphere by the polyol method. Poly(N-vinylpyrrolidone) (PVP, $M_w = 10,000, 29,000, \text{ and } 40,000 \text{ g mol}^{-1}$) was used as a capping agent to hinder surface oxidation and diethylene glycol (DEG) was utilized as a reaction medium. Polyol synthesis at 140 °C (284 °F) for 1 h gave rise to relatively uniform PVP-coated Cu nanoparticles. The average particle size increased with PVP molecular weight. Moreover, electronic microscopy images of the synthesized Cu nanoparticles show that regardless of the PVP molecular weight, an amorphous layer is present on the surface of each nanoparticle. Given that PVP is generally invisible under an electron microscope, we consider that the surface amorphous layer solely represents the surface layer of CuO. Before the nucleation and growth of the nanoparticles, the Cu ions dissolved in the polyol medium bond to the PVP; specifically lone pairs of electrons on the oxygen atoms in the polar groups of the PVP monomer unit are donated to an sp hybrid orbital of the Cu^{2+} ions to form a Cu–O coordination.^[4,5]

X-ray spectral analyses in the Cu $2p_{3/2}$ region proved that the surface oxide layer becomes

thinner as the PVP molecular weight increases. Moreover, the finding suggests that the capping molecules on the Cu surface take on different conformations depending on the PVP molecular weight. The longer PVP chains are more effectively adsorbed on the Cu surface compared to shorter chains. In other words, the density of sites at which PVP attaches to the Cu surface increases with increasing PVP chain length. Hence PVP with a higher molecular weight is more densely packed on the Cu surface (**Figure 1b**), whereas PVP with a lower molecular weight is loosely packed on the Cu surface due to a lower density of attachment sites (**Figure 1a**). These findings suggest that a densely packed layer of adsorbed PVP on the Cu surface can hinder access of the oxygen atoms to the metal during the particle synthesis, resulting in reduced surface oxidation and thus to a thinner oxide layer.

The thickness of the surface oxide layer on individual Cu nanoparticles significantly influences the microstructure and physical properties of the resulting consolidated particulate film. In the present work, we monitored the evolution of the conductivity of Cu granular films prepared from Cu nanoparticles with different surface oxide layer thicknesses as a function of heat-treatment temperature; the

results are listed in **Figure 2**. For each annealing temperature, the resistivity of the film prepared using Cu nanoparticles with a higher molecular weight PVP is lower than that of the film prepared using Cu nanoparticles with a lower molecular weight PVP. The development of a more conductive film when Cu particles, prepared using a higher molecular weight PVP, are annealed at the same temperature as those prepared using a lower molecular weight PVP indicates that the particles with a thinner surface oxide layer undergo coalescence to a greater extent during a given annealing time. The amount and type of PVP chemisorbed on the Cu particles could potentially affect the sintering process by interrupting the migration of Cu atoms into neck regions. However, thermal gravimetric analysis revealed that the amounts of adsorbed PVP were nearly identical for the three types of Cu nanoparticles (~1.5 wt %) and that thermal decomposition of the PVP commenced at around 200 °C (392 °F) regardless of the polymer molecular weight; these findings indicate that the differences in the sintering behavior are not due to variations in the amount and type of PVP chemisorbed on the Cu nanoparticles.

The distinct sintering kinetics of the Cu nanoparticles with different surface oxide layer thicknesses can be attributed to the char-

acteristics of the particles, such as their size and melting point (T_m). Smaller particles are expected to show faster sintering kinetics due to a reduced mass diffusion length. However, the experimental results are not in line with this expectation. Specifically, the Cu nanoparticles prepared using a higher molecular weight PVP (i.e., a thinner surface layer) have the largest particle size (~60 nm) but the fastest sintering kinetics. This finding leads us to conclude that the observed differences in the sintering kinetics are associated with variations in the thickness of the surface oxide layer rather than the particle size. It is generally recognized that the sintering process occurs at a temperature that is around 80% of the melting point. The melting point of bulk CuO (T_m ~1,330 °C or 2,426 °F) is higher than that of bulk Cu (T_m ~830 °C or 1,526 °F). Scanning electron microscopy microstructural analysis results indicate that, compared to the Cu film prepared from Cu nanoparticles with a thicker surface oxide layer, the Cu film prepared from nanoparticles with a thinner surface oxide layer is much denser, forming more particle-particle junctions when heat-treated at the same temperature. This enhanced sintering process is also supported by exothermic peaks in a differential scanning calorimetry analysis. The formation of necks between particles involves surface diffusion of unstable surface atoms, which is observed as the exothermic peaks.^[6,7] The exothermic peak position shifts toward a lower temperature as the molecular weight of PVP increases (i.e., the surface oxide layer becomes thinner), indicating that the sintering process for the Cu nanoparticle with a thinner oxide layer is initiated at a lower heat-treatment temperature. The thickness of the surface oxide layer thus plays a critical role in determining the resistivity of the Cu granular film, predominating over the particle size effect.

To demonstrate the applicability of the Cu nanoparticles with controlled surface chemistry, we prepared the inkjet-printable conductive inks. **Figure 3** shows complex conductive patterns printed on a flexible polyimide substrate using the Cu nanoparticles prepared with PVP of 40,000 g mol⁻¹ in molecular weight. Solvent evaporation from the printed single ink droplet produces a spherical dot pattern of diameter 120 nm. The line pattern is generated by reducing the dot-to-dot distance. The separated dots begin to merge at 80 nm, and printing at an inter-dot distance of 60 nm results in a continuous line with a 130 nm linewidth and relatively smooth edge definition. To our knowledge, this represents

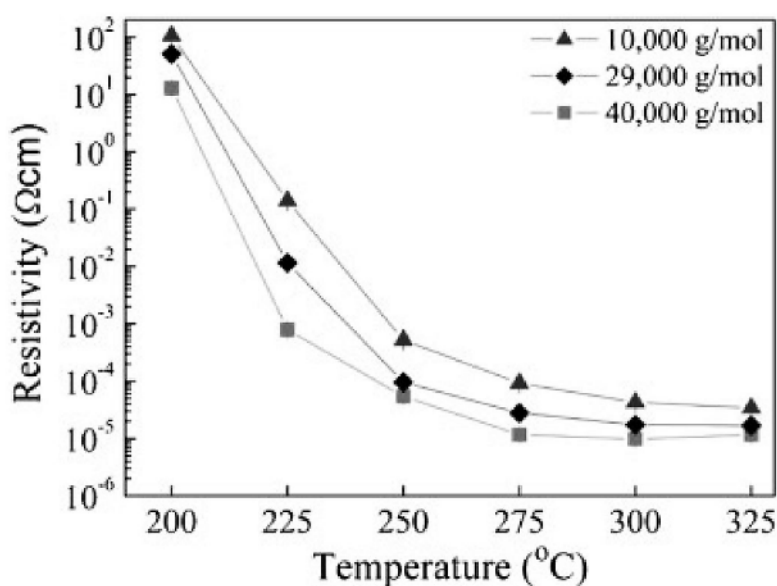


Figure 2: Resistivity of the Cu conductive film as a function of heat treatment temperature. The inkjet-printed Cu nanoparticulate films were heat-treated at various temperatures between 200 °C and 325 °C (392 °F and 619 °F) under vacuum (103 Torr).

the first attempt to directly write a conductive Cu pattern on a plastic substrate via inkjet printing of ink containing Cu nanoparticles. The conductive features exhibited relatively low electrical resistivity ($\sim 11 \mu\Omega\cdot\text{cm}$) after heat treatment at $275 \text{ }^\circ\text{C}$ ($527 \text{ }^\circ\text{F}$) for 60 min. Thus, the Cu-nanoparticle-based conductive ink used here provides a convenient and low-cost method for fabricating conductive features. Especially, the ability to directly write conductive Cu patterns provides new opportunities for the fabrication of flexible printed electronics such as organic light-emitting diodes, organic thin-film transistors, and solar cells.

CONCLUSIONS

We have controlled the thickness of the surface oxide layer on Cu nanoparticles by varying the molecular weight of PVP added to the reaction mixture used to generate the nanoparticles. The minimum thickness of the amorphous CuO and chemisorbed PVP layers was determined to be 1.6 nm and was obtained using PVP with a molecular weight of $40,000 \text{ g mol}^{-1}$ or higher. The molecular weight of the PVP capping agent determines its conformation when chemisorbed on the Cu surface, which significantly influences the formation of the surface oxide layer. In addition, our results confirm that the surface oxide layer thickness is the

predominant factor determining the electrical conductivity of the Cu nanoparticle granular film obtained by annealing nanoparticle assemblies. Importantly, we established that the synthesized Cu nanoparticles with controlled surface chemistry could be used to directly write conductive features on a plastic substrate.

EXPERIMENT

Copper nanoparticles 35–60 nm in size were synthesized in an ambient atmosphere by the polyol method. Details of the synthesis procedure were described previously.^[8] Poly(N-vinylpyrrolidone) ($M_w = 10,000, 29,000,$ and $40,000 \text{ g mol}^{-1}$, Sigma–Aldrich), acting as a capping molecule to hinder the formation of an oxide layer, was dissolved in diethyleneglycol (99%, Sigma–Aldrich). Sodium phosphinate monohydrate ($\text{NaH}_2\text{PO}_2\cdot\text{H}_2\text{O}$; Junsei), used as a reducing agent, was added to the DEG solution and the solution was heated to a reaction temperature of $140 \text{ }^\circ\text{C}$ ($284 \text{ }^\circ\text{F}$). An aqueous solution of copper (II) sulfate pentahydrate (98%; Sigma–Aldrich) was then injected into the hot reaction medium via a syringe pump at a rate of 2 mL/min . In the synthesis step, the volume ratio of DEG to water was 7.3:1. After 1 h of reaction, the solution was cooled to room temperature, and the particles were separated by centrifugation and then washed with methanol.

Conductive ink incorporating the synthesized Cu nanoparticles was prepared using a mixed solvent comprised of ethylene glycol (EG), 2-methoxyethanol (MeEtOH), and methyl alcohol (MeOH). The weight ratio of EG:MeEtOH:MeOH was 5:4:1. The copper nanoparticles were dispersed in the premixed solvent, and the mixture was subjected to ball milling for 12 h. The resulting ink was filtered through 5 mm nylon mesh before use. The solid loading of the ink was 20 wt%. The Cu conductive ink was printed onto a polyimide substrate (Kapton, Dupont) in an ambient atmosphere using an inkjet printer. The printer setup consisted of a drop-on-demand piezoelectric inkjet nozzle manufactured by Microfab Technologies (Plano, TX), and the diameter of the nozzle was 30 μm . Uniform ejection of the droplets was achieved by applying a 25 V pulse lasting 10 ms at a frequency of 400 Hz. The diameter and velocity of the ejected droplets were about 50 μm and 3 m s^{-1} , respectively. The inkjet-printed Cu nanoparticulate films were heat-treated at various temperatures between $200 \text{ }^\circ\text{C}$ and $325 \text{ }^\circ\text{C}$

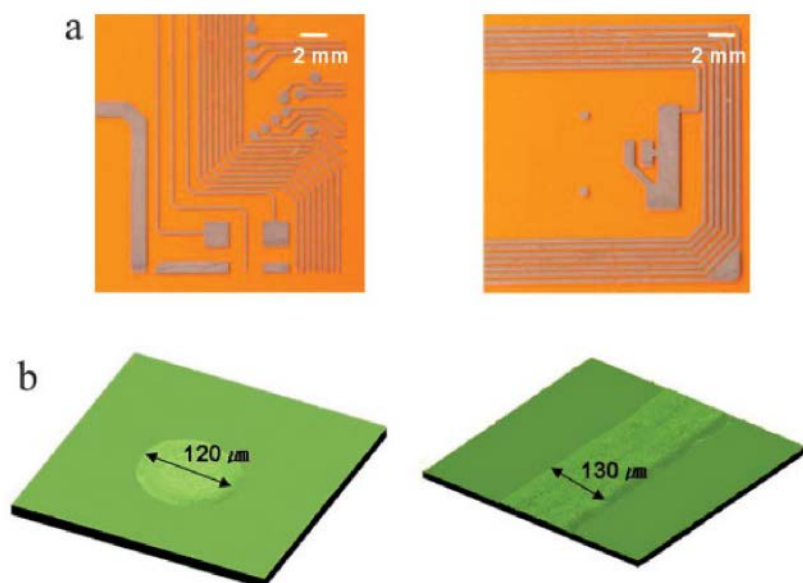


Figure 3: a) Cu conductive patterns inkjet printed on polyimide substrates using Cu nanoparticles with the thinnest oxide layer; b) confocal images of a single ink droplet after drying and a single printed line.

(392 °F and 617 °F) under vacuum (10^3 Torr) for 60 min to form inter-particle connections for developing electrical conductivity.

The three-dimensional morphology and microstructure of the inkjet-printed Cu conductive patterns were observed by confocal microscopy (LEXT OLS3000, Olympus). The particle size was evaluated by laser light scattering and image analysis based on the SEM image.

REFERENCES

- [1] Kim, D. et al. (2006). Direct writing of silver conductive patterns: Improvement of film morphology and conductance by controlling solvent compositions. *Applied Physics Letters*. DOI: 10.1063/1.2424671.
- [2] Wu, Y. et al. (2005). High-Performance Organic Thin-Film Transistors with Solution-Printed Gold Contacts. *Advanced Materials*. DOI: 10.1002/adma.200400690.
- [3] Liu, P. et al. (2006). Enabling Gate Dielectric Design for All Solution-Processed, High-Performance, Flexible Organic Thin-Film Transistors. *Journal of the American Chemical Society*. DOI: 10.1021/ja060620l.
- [4] Yin, B. et al. (2003). Electrochemical Synthesis of Silver Nanoparticles under Protection of Poly(*N*-vinylpyrrolidone). *The Journal of Physical Chemistry B*. DOI: 10.1021/jp0349031.
- [5] Washio, I. et al. (2006). Reduction by the End Groups of Poly(vinyl pyrrolidone): A New and Versatile Route to the Kinetically Controlled Synthesis of Ag Triangular Nanoplates. *Advanced Materials*. DOI: 10.1002/adma.200600675.
- [6] Kim, D. and Moon, J. (2005). Highly Conductive Ink Jet Printed Films of Nanosilver Particles for Printable Electronics. *Electrochemical and Solid-State Letters*. DOI: 10.1149/1.2073670.
- [7] Moon, K.-S. et al. (2005). Thermal behavior of silver nanoparticles for low-temperature interconnect applications. *Journal of Electronic Materials*. DOI: 10.1007/s11664-005-0229-8.
- [8] Park, B.K. et al. (2007). Synthesis and size control of monodisperse copper nanoparticles by polyol method. *Journal of Colloid and Interface Science*. DOI: 10.1016/j.jcis.2007.03.039.